Ultrasonics 91 (2019) 10–18

Contents lists available at ScienceDirect

Ultrasonics

journal homepage: www.elsevier.com/locate/ultras

Kriging model to study the dynamics of a bubble subjected to tandem shock waves as used in biomedical applications

Ángel Gutiérrez-Prieto[a], Miguel de Icaza-Herrera[b], Achim M. Loske[b,*], Eduardo Castaño-Tostado[c]

[a] Licenciatura en Matemáticas Aplicadas, Facultad de Ingeniería, Universidad Autónoma de Querétaro, C.U., Cerro de las Campanas s/n, 76010 Querétaro, Qro., Mexico
[b] Centro de Física Aplicada y Tecnología Avanzada, Universidad Nacional Autónoma de México, Boulevard Juriquilla 3001, 76230 Querétaro, Qro., Mexico
[c] Facultad de Química, Universidad Autónoma de Querétaro, C.U., Cerro de las Campanas s/n, 76010 Querétaro, Qro., Mexico

ARTICLE INFO

Keywords:
Tandem shock waves
Biomedical applications
Cavitation
Numerical simulation
Metamodel
Kriging

ABSTRACT

The purpose of this work was to develop a metamodel (Kriging model) to identify the most important input parameters of shock wave pressure profiles as used in biomedical applications without solving a large number of differential equations. Shock wave-induced cavitation is involved in several biological effects. During bubble collapse, secondary shock waves and microjets are formed. For some applications, it is desirable to enhance this phenomenon by applying a second shock wave before bubble collapse; however, the delay between the leading shock wave and the second pressure pulse has yet to be optimized. This optimization can be done using numerical analysis. A metamodel that predicts the most convenient ranges for the input variables and provides information on the joint effects between the input variables was tested. Because the metamodel is an analytical expression, running it fifty thousand times and analyzing variables, such as the pressure amplitude, delay between pulses, and pressure rise time, was fast and easy. Furthermore, this method can be a helpful tool to study the joint effect between the input variables and reduce the computation time. The metamodel can also be adapted to analyze simulations based on equations different from the Gilmore-Akulichev formulation, which was used in this study.

1. Introduction

The high efficacy of shock waves in treating patients with urinary calculi, a technique referred to as extracorporeal shock wave lithotripsy (SWL), motivated the use of such shock waves as an alternative treatment for stones in the gallbladder, the common bile duct, the pancreatic duct and the salivary gland ducts. There is a large variety of devices (lithotripters) to perform SWL, which all consist of a shock wave generator, a coupling device, a patient treatment table, and imaging systems (ultrasound and/or fluoroscopy). Extracorporeally generated shock waves enter the body through a fluid-filled cushion and are focused on the calculus by means of lenses, reflectors or spherically curved shock wave sources. From several hundred to a few thousand shock waves may be required to pulverize a stone. In urological SWL, stone debris passes through the urinary tract and is eliminated during the days following the treatment. Research has been focused on designing shock wave sources to emit pressure profiles that enhance stone comminution without increasing tissue damage [1]. Remarkably, shock waves are currently also used in a variety of clinical applications different from SWL, such as the treatment of the nonunion of long bones, plantar fasciitis, calcaneal spurs, tendinopathy of the shoulder, Achilles tendinopathy, epicondylitis of the elbow, heart diseases, erectile dysfunction, and chronic pelvic pain syndrome. Other promising uses are the shock wave-mediated transformation of bacteria and fungi, as well as human cell transfection [1]. The typical pressure waveforms used in biomedical applications consist of a 10–150 MPa compression pulse with a duration t^+ of approximately 0.5–3 μs and a rise time between a few nanoseconds and approximately 500 ns, followed by a decompression pulse of up to −25 MPa with a duration of approximately 2–20 μs. The duration t^+ is defined as the time from the instant when the pressure exceeds 50% of the peak positive pressure for the first time to the instant when the pressure drops again to this value. Energy flux densities vary between 0.2 and 2.0 mJ/mm^2 [1–3].

One of the most important stone comminution mechanisms during SWL is acoustic cavitation, i.e., the growth and collapse of bubbles in liquids resulting after a sudden pressure change, which plays a crucial role in obtaining small fragments. Microbubbles existing in the fluid close to the focal zone of a lithotripter suffer a forced collapse after the passage of the positive peak of each shock wave. An instant later, the high pressure inside the compressed bubbles and the trailing tensile

* Corresponding author.
E-mail address: loske@fata.unam.mx (A.M. Loske).

https://doi.org/10.1016/j.ultras.2018.07.005
Received 26 May 2018; Received in revised form 12 July 2018; Accepted 12 July 2018
Available online 18 July 2018
0041-624X/

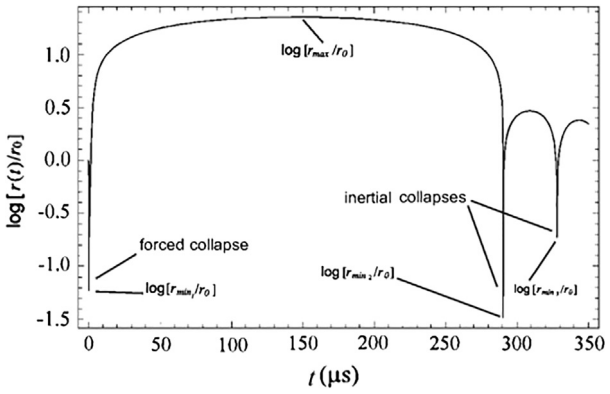

Fig. 1. Base 10 logarithm of the bubble radius $r(t)$ normalized by the initial bubble radius (r_o = 70 μm) plotted as a function of time after the passage of a typical lithotripter shock wave (positive pressure amplitude = 100 MPa). The second bubble collapse occurred at approximately 290 μs.

phase of the shock wave trigger their fast growth. As the volume of the bubbles increases, the pressure inside them decreases until they suffer a violent inertial collapse after hundreds of microseconds (Fig. 1). Bubble collapse is affected by the surrounding fluid and is generally asymmetrical. As a consequence, the pressure difference outside the bubble creates a high-speed fluid microjet that burrows through the bubble [4]. Secondary shock waves may be produced by the collision between the microjet and the inward-moving wall of each bubble. These secondary shock waves have a short range. Nevertheless, this phenomenon is considered to be an additional mechanism for increasing the efficacy of calculi disintegration. Even at positive pressure amplitudes of only 10 MPa, liquid microjets are emitted in the direction of the incoming shock wave [5]. The larger a bubble grows, the more violent its collapse will be. Shock wave-induced microjets are also useful to introduce large-sized molecules into cells for therapeutic applications and the genetic transformation of bacteria and fungi [1,5].

Bubble dynamics depend on several factors, such as the impinging pressure waveform, the content of dissolved gases, the viscosity, the surface tension, and the existence of cavitation nuclei. Cavitation may also be responsible for undesired effects on tissue. Fortunately, cavitation is less violent if the bubbles are constrained in soft tissue [1,6].

It is known that bubble collapse can be significantly enhanced if a second shock wave arrives just before the bubbles start to collapse [3,7]. Tandem shock waves is the name given to the production of two shock waves with a delay of approximately 10–900 μs between them; they have been generated using electrohydraulic shock wave sources with composite and confocal reflectors, as well as with two spark gaps [7–11], combined electrohydraulic and piezoelectric shock wave generators [12], and modified piezoelectric shock wave sources [13]. In vivo results have demonstrated that tandem shock waves may dramatically reduce SWL treatment times without increasing tissue damage [14,15]. Furthermore, exposing suspensions of gram-negative (*Escherichia coli*) and gram-positive (*Listeria monocytogenes*) bacteria to tandem shock waves significantly enhanced bacterial inactivation [16]. More recently, the genetic transformation of bacteria and filamentous fungi was increased by using tandem shock waves instead of conventional single-pulse shock waves [17,18]. As a further development, so-called "modified tandem shock waves", where a conventional shock wave (p_c) is followed by a relatively slow pressure pulse (p_s), were proposed [19] (see Fig. 2(a)). Because bubble collapse lasts tenths of microseconds, when using standard tandem shock waves, the negative tail of the second shock wave arrives during the inertial collapse. This effect can reduce the bubble collapse energy to a certain extent. If the second pressure pulse has a longer positive pulse duration, the positive pressure will be compressing the bubble during a longer time of its collapse, increasing the collapse energy and, as a consequence, enhancing

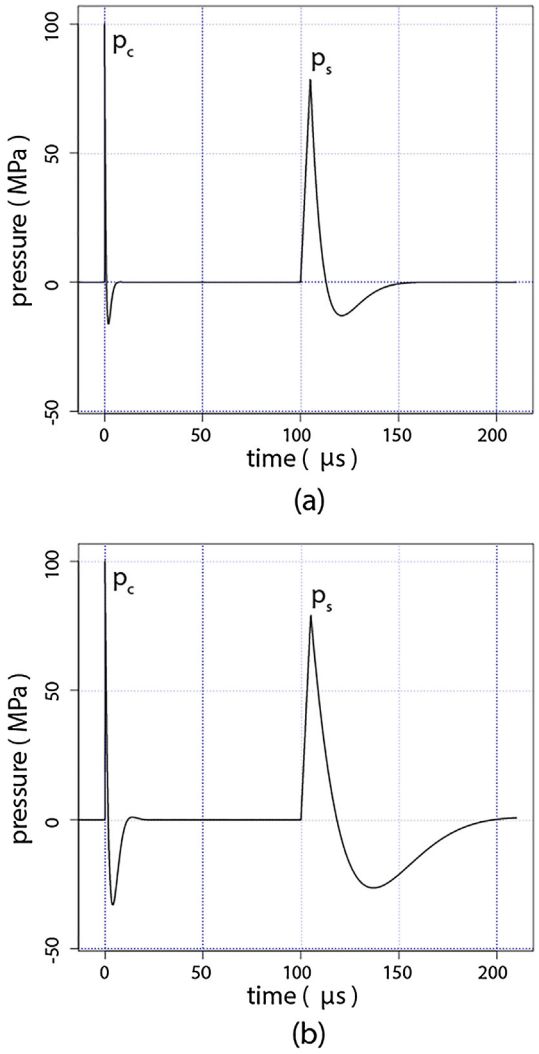

Fig. 2. Plots of two modified tandem shock waves, generated by substituting (a) α_1, ω_1 and (b) α_2, ω_2 in Eqs. (2) and (3). In both cases, t_r = 5 μs, p_1 = 100 MPa, and p_2 = 80 MPa. For clarity, Δt was chosen to be 100 μs.

microjet and secondary shock wave emissions.

The optimal delay between the leading shock wave and the second pressure wave depends on the specific application and in many cases has not been established. In vitro stone phantom fragmentation [13], dual passive cavitation detectors [20], recording of images with high-speed cameras [1], and pressure waves emitted from bubble collapses using hydrophones [1,21] may be helpful. Nevertheless, many experiments are required because the location and time of appearance of cavitation bubbles are of a statistical nature. To reduce the experimentation time, computer modeling of the dynamics of a bubble subjected to tandem shock waves at several different delays and pressure profiles has been useful [19,22]. In a previous publication, the influence of modified tandem shock waves on the collapse energy of a single bubble immersed in water was analyzed using a numerical simulation [19]. The results were compared with the dynamics of the same bubble subjected to standard tandem shock wave profiles. The main conclusion was that modified tandem shock waves could significantly improve SWL outcomes compared to those for standard tandem waves. In a second study, a numerical simulation was used to show that stress and cavitation can be enhanced using a pressure pulse with a long full width at half maximum, which reaches the urinary stone within hundreds of microseconds after two 20 μs-delayed initial shock waves [22].

Modified tandem shock waves can be generated using piezoelectric

shock wave sources; however, more information on the influence of the delay, the rise time, the peak positive pressure and the duration of the second shock wave on the dynamics of bubbles subjected to these pressure variations is required to design the optimal pressure profile for specific biomedical applications. Because many numerical simulations are required to obtain this information, the aim of this study was to develop a surrogate model (metamodel) to be used in computer simulations instead of the Gilmore-Akulichev equation and to identify the most important input factors of the pressure profile.

The paper is organized as follows: Initially, a few basic concepts of the numerical simulation of the dynamics of a single bubble subjected to shock waves, modeled by the Gilmore-Akulichev formulation, are explained. A brief description of statistical modeling, the metamodel, and the sensitivity analysis follows. The results section presents the most important findings, showing the potential of the metamodel proposed in this article. Finally, a discussion of the results and the main conclusions, including comments on the limits and advantages of the novel methodology, are given.

2. Fundamentals

2.1. Numerical simulation of bubble dynamics after exposure to tandem shock waves

In this section, we briefly describe the model for simulating radial bubble pulsations of a single spherical air bubble subjected to conventional (single-pulse) shock waves, tandem shock waves, and modified tandem shock waves in water. The most popular equation to obtain the radius r as a function of time of a spherical bubble exposed to a shock wave as produced by medical equipment is the Gilmore-Akulichev formulation [23]:

$$r\left(1-\frac{u}{c}\right)\frac{du}{dt}+\frac{3}{2}\left(1-\frac{u}{3c}\right)u^2=h\left(1+\frac{u}{c}\right)+\frac{ru}{c}\left(1-\frac{u}{c}\right)\frac{dh}{dr}, \tag{1}$$

where $u = dr/dt$ is the bubble wall velocity; c is the speed of sound in water; $h(p)$ is the enthalpy difference between the liquid at a pressure p and the undisturbed pressure far away from the bubble; and h and c are determined using an equation from Tait [19,23]. The influence of a pressure profile p on Eq. (1) is a central question of underwater shock wave theory. The Gilmore-Akulichev equation considers the compressibility of the liquid. Its main assumption is that the initial bubble radius is much smaller than the driving pressure pulse length (approximately 2.5 mm). Shock waves are “ultrasonic” transformations connecting states under adiabatic conditions because the changes are so fast that no heat exchange is possible. This condition is used in the Gilmore-Akulichev formulation in the connection between the pressure and density. During the shock transformation, only the initial temperature is considered. Furthermore, diffusion of gas into the bubble, or from the bubble, was not included in this model because the expansion phase of the bubble is mainly driven by the inertia of the liquid.

The conventional shock wave pressure profile, denoted by $p_c(t)$, was modeled as a function of t by Church [23] as follows:

$$p_c(t)=2p_1e^{-\alpha t}\cos\left(\omega t+\frac{\pi}{3}\right)\quad for\quad t\geq 0 \tag{2}$$

where the decay parameter α and the angular frequency $\omega = 2\pi f$ are constants and p_1 is the positive peak pressure. A pressure profile $p_s(t)$, referred to as a “slow” pulse, has been defined as follows [19]:

$$p_s(t)=\begin{cases}\left(\frac{t}{t_r}\right)p_2 & for\quad 0\leq t<t_r\\ 2p_2e^{-\alpha t/8}\left(\frac{\omega t}{8}+\frac{\pi}{3}\right) & for\quad t\geq t_r\end{cases} \tag{3}$$

In this article, t_r will be called the induction time, and p_2 is a parameter related to the positive and negative amplitude of $p_s(t)$.

Two values were used for both the decay constant ($\alpha_1 = 9.1 \times 10^5\ s^{-1}$; $\alpha_2 = 3.5 \times 10^5\ s^{-1}$) and the frequency ($f_1 = 83.3$ kHz; $f_2 = 50.0$ kHz). In the early days of SWL, the pressure pulse was modeled using (α_1, ω_1) [23]; however, more accurate pressure measurements obtained with newer hydrophones revealed that the negative part of the pressure waveform has a longer duration than what was initially assumed [24]. Therefore, a more realistic temporal profile is obtained by substituting the original parameters (α_1, ω_1) with (α_2, ω_2).

As shown in Fig. 2(a), tandem shock waves are defined as a $p_c(t)$ waveform, followed after a delay Δt by another $p_c(t)$ pulse, while modified tandem shock waves have been modeled as a $p_c(t)$ waveform, followed after a delay by a $p_s(t)$ waveform. Currently, no experimental studies showing that modified tandem shock waves are more efficient than conventional tandem shock waves have been published. Initial computer simulations have revealed that, under certain conditions, modified tandem shock waves appear to be significantly more efficient than conventional tandem shock waves are [19]. Nevertheless, more details on the interactions between the parameters involved would be helpful for designing experimental studies. Therefore, only modified tandem shock waves are analyzed here.

During numerical simulations, the maximum radius r_{max} (Fig. 1) achieved by a bubble subjected to a particular pressure profile, has been used as a representative measure of the bubble-collapse intensity and its potential effects (for instance, the fragmentation efficacy) [25]. However, when analyzing the behavior of a bubble subjected to tandem shock waves, r_{max} should not be used as an indirect measure of the bubble-collapse energy because the second shock wave may arrive after the bubble has acquired r_{max}. Therefore, for numerical simulations, the minimum radius (r_{min}) achieved during bubble collapse has been proposed as the representative measure to assess the potential efficiency of a specific pressure waveform. As shown in Fig. 1, if the bubble is subjected to a single $p_c(t)$ waveform, the minimum radius is achieved during the second bubble collapse (r_{min2}). If a modified tandem shock wave, i.e., a $p_c(t)$ waveform followed by a $p_s(t)$ waveform, impinges on the bubble, then r_{min} can occur at either the second (r_{min2}) or at the third (r_{min3}) bubble collapse, depending on the time delay between the pressure pulses composing the modified tandem shock waves.

2.2. Statistical modeling

Eqs. (1)–(3) show the theoretical model used in computer simulations to analyze the bubble evolution when submitted to modified tandem shock waves. Clearly, for specific α and ω values, this model is crucial to perform a sensitivity analysis in relation to how r_{min} changes as the parameter configuration (Δt, p_2, t_r) changes, considering an initial bubble radius (r_0). However, to gain knowledge of this scenario, there are two main concerns. One is the many combinations of these parameters. Therefore, using the theoretical model is a complicated task, mainly due to the required simulation time for each parameter change. For instance, the time required to obtain a graph showing the dynamics of a bubble subjected to a modified tandem shock wave, using a personal computer (Intel core i7-3770 CPU @ 3.4 GHz x 8 and 3.8 GB RAM) was approximately 8 s. Obtaining data for 50,000 scenarios, as will be presented later in this article, would take more than 4 days and 15 h, without considering the time to vary the parameters either “manually” or by designing software to do so. The methodology described here solves this task in a few seconds. The second concern is that, traditionally, parameters are changed in a one-parameter-at-a-time strategy, a simple but inefficient computer design strategy imposed by the time limitation and dimensional difficulties in the interpretation of multiple effects.

Considering these two concerns, we propose the use of a Kriging model [26], i.e., a statistical and simplified version of the original model, a metamodel that is much faster to compute than the theoretical model is and that provides an easier sensitivity analysis from simultaneous changes in the parameter configuration. Three parameters (Δt, p_2, t_r) were selected to generate a uniform statistical design to

obtain a set of r_{min} values. The boundaries of the experimental design were set between the minimum and maximum values that make sense according to the physics of bubble dynamics.

2.3. The Kriging model

Kriging is a versatile statistical tool to model how a response variable Y changes as a function of a vector $\boldsymbol{x}$ of dimension d. Kriging builds a model using a Gaussian process governed by prior covariances, that is,

$$Y(\boldsymbol{x}) = \mu + z(\boldsymbol{x}),$$

where μ is a parameter and $z(\boldsymbol{x})$ is a Gaussian process with a mean 0 and covariance function

$$c(\boldsymbol{x}_i, \boldsymbol{x}_j) = \sigma^2 \exp\left\{-\sum_{k=1}^{d} \theta_k \, |x_{ik} - x_{jk}|^2\right\} \tag{4}$$

where $\boldsymbol{x}_i$ and $\boldsymbol{x}_j$ denotes two specific vectors $\boldsymbol{x}$ and $\theta_k \geq 0$. In applications, $\boldsymbol{\gamma} = (\theta_1, \cdots \theta_d, \sigma^2)^T$ is unknown. The statistical problem is to obtain $\boldsymbol{\gamma}$ from the set $\boldsymbol{Y} = \{Y(\boldsymbol{x}_i), i = 1, \cdots, n\}$, where $\{\boldsymbol{x}_i, i = 1, \cdots, n\}$ are selected to efficiently obtain estimates $\hat{\mu}$ and $\hat{\boldsymbol{\gamma}}$; typically, $\{\boldsymbol{x}_i, i = 1, \cdots, n\}$ is a random uniform sample value in the $\boldsymbol{x}$ region. Optimal estimates $\hat{\mu}$ and $\hat{\boldsymbol{\gamma}}$ are found using statistical theory and numerical algorithms. Then, letting $\mathbf{b}(\boldsymbol{x}) = (\hat{c}(\boldsymbol{x}, \boldsymbol{x}_1), \cdots, \hat{c}(\boldsymbol{x}, \boldsymbol{x}_n))$, where $\hat{c}(\boldsymbol{x}, \boldsymbol{x}_i)$ is

$$\hat{c}(\boldsymbol{x}, \boldsymbol{x_i}) = \hat{\sigma}^2 \exp\left\{-\sum_{k=1}^{d} \widehat{\theta_k} \, |x_k - x_{ik}|^2\right\},$$

the best linear unbiased predictor of $Y(\boldsymbol{x})$ is the following:

$$\hat{Y}(\boldsymbol{x}) = \hat{\mu} + \boldsymbol{b}(\boldsymbol{x})\boldsymbol{C}^{-1}(\hat{\boldsymbol{\gamma}})(\boldsymbol{Y} - 1_n\hat{\mu}), \tag{5}$$

where $\boldsymbol{C}(\hat{\boldsymbol{\gamma}})$ is the estimated value of the correlation matrix (4) of the Gaussian process z($\boldsymbol{x}$).

Eq. (5) represents a Kriging-type metamodel for $Y(\boldsymbol{x})$. For more details consult [26]. Notably, Kriging is only one alternative for obtaining a metamodel. Other metamodels may be used [27].

2.4. Sensitivity analysis

To compute the influence from a subset $i_1 \cdots i_s$ of the components of the configuration $\boldsymbol{x}$, considering that $\hat{Y}(\boldsymbol{x})$ is a Riemann-integrable function, and can be decomposed as [26],

$$\hat{Y}(\boldsymbol{x}) = g_0 + \sum g_l(x_l) + \sum_{l<k} g_{lk}(x_l, x_k) + \cdots + g_{1\ldots s}(x_1, \cdots, x_s),$$

where

$$\int \hat{Y}(\boldsymbol{x}) d\boldsymbol{x} = g_0$$

$$\int \hat{Y}(\boldsymbol{x}) \prod_{k \neq l} dx_k = g_0 + g_l(x_l)$$

$$\int \hat{Y}(\boldsymbol{x}) \prod_{k \neq l,m} dx_k = g_0 + g_l(x_l) + g_m(x_m) + g_{lm}(x_l, x_m).$$

Then,

$$\int \hat{Y}(\boldsymbol{x})^2 d\boldsymbol{x} = g_0^2 + \sum_l \int g_l^2(x_l) dx_l + \sum_{l<m} \int g_{lm}{}^2(x_l, x_m) dx_l dx_m + \cdots + \int g_{12\ldots s}{}^2(x_1, \cdots, x_s).$$

The total variance, denoted by D, and partial variances, denoted by $D_{i_1 \cdots i_s}$, are defined as follows:

$$D = \int \hat{Y}(\boldsymbol{x})^2 d\boldsymbol{x} - g_0{}^2, \; D_{i_1 \cdots i_s} = \int g_{i_1 \cdots i_s}{}^2(x_{i_1}, \cdots, x_{i_s}) dx_{i_1} \cdots dx_{i_s},$$

where the ratio

$$\frac{D_{i_1 \cdots i_s}}{D}$$

is the so-called Sobol's index for the subset $i_1 \cdots i_s$ to weight its influence over $\hat{Y}(\boldsymbol{x})$. In this study, we computed Sobol's indices for subsets of $\boldsymbol{x}$ with $S = 1$ and $S = 2$.

Table 1
Uniformly distributed values of the parameters for the small bubble ($r_0 = 7$ μm).

Run	p_2	t_r	Δt	r_0
1	32.1743	4.0874	702.928	0.007
2	78.3925	0.70229	546.956	0.007
3	57.3289	6.50672	16.2127	0.007
4	55.7912	8.10547	326.206	0.007
5	**90.774**	**8.44257**	**968.492**	**0.007**
6	61.545	7.67646	154.457	0.007
7	76.8055	4.51719	114.268	0.007
8	44.6	8.29584	419.947	0.007
9	52.6702	6.30664	879.651	0.007
10	33.3547	9.12334	445.295	0.007
11	39.0962	5.7035	192.563	0.007
12	34.7654	2.50038	72.909	0.007
13	65.4548	0.31844	209.989	0.007
14	48.7899	7.0875	586.303	0.007
15	60.2957	2.30161	522.658	0.007
16	**40.2721**	**8.70879**	**841.039**	**0.007**
17	**97.7678**	**8.91082**	**59.5763**	**0.007**
18	83.9493	1.47971	170.541	0.007
19	75.3981	9.30729	896.103	0.007
20	30.7532	3.67136	485.995	0.007
21	67.1376	5.92336	249.035	0.007
22	**41.9348**	**4.91607**	**784.876**	**0.007**
23	68.3619	3.48393	934.532	0.007
24	82.5788	9.88478	509.548	0.007
25	58.6097	1.69896	725.743	0.007
26	95.038	3.86503	231.964	0.007
27	51.3955	9.5274	133.159	0.007
28	36.1253	7.3327	745.144	0.007
29	89.3283	5.3079	600.816	0.007
30	63.1106	9.70209	644.831	0.007
31	99.161	3.23469	661.34	0.007
32	70.3077	1.28612	800.352	0.007
33	80.8499	7.9063	268.586	0.007
34	37.6703	1.08334	286.777	0.007
35	50.2584	2.09276	404.654	0.007
36	80.0542	2.80691	859.059	0.007
37	64.1366	4.66178	915.923	0.007
38	92.4714	0.13133	391.858	0.007
39	45.9944	4.30275	95.1718	0.007
40	74.0168	5.48076	308.937	0.007
41	**96.4243**	**5.06294**	**819.165**	**0.007**
42	86.7357	6.92705	367.608	0.007
43	72.567	7.49476	469.674	0.007
44	93.6448	6.72246	684.071	0.007
45	43.2509	2.71082	566.31	0.007
46	**88.2544**	**1.90855**	**34.8417**	**0.007**
47	47.2302	0.46793	629.721	0.007
48	85.1194	6.09141	760.032	0.007
49	71.4219	3.09628	346.767	0.007
50	54.2307	0.87053	955.207	0.007

3. Methods

To be consistent with previous studies [19], the bubble dynamics were simulated using Eqs. (1)–(3) with two different initial bubble radii r_0 (7 and 70 μm) and the two sets of α and ω values previously mentioned. Using a uniform design, we selected 50 points (Δt, p_2, t_r) in R^3 with the respective ranges for each input variable (see Tables 1 and 2). The simulation was run 50 times for each scenario. The first shock wave (p_c) was always modeled using Eq. (2) with $p_1 = 100$MPa and a rise time of zero. The second pressure pulse (p_s) was modeled according to Eq. (3), varying p_2 between 30 and 100 MPa, and the induction time (t_r)

Table 2
Uniformly distributed values of the parameters for the large bubble ($r_0 = 70\,\mu m$).

Run	p_2	t_r	Δt	r_0
1	82.2943	4.8818	397.415	0.07
2	61.6755	2.30093	553.81	0.07
3	74.6157	4.08776	78.4913	0.07
4	51.7209	1.31096	676.042	0.07
5	96.5162	7.83797	931.382	0.07
6	66.0051	1.50448	431.088	0.07
7	46.184	2.08798	609.837	0.07
8	76.6433	1.91458	874.047	0.07
9	48.8987	6.69094	22.2189	0.07
10	93.646	3.46754	193.16	0.07
11	95.2259	1.70765	455.574	0.07
12	63.1359	5.49873	989.71	0.07
13	66.9554	9.88818	689.331	0.07
14	33.2952	3.28411	652.244	0.07
15	89.5678	2.6926	789.845	0.07
16	79.4779	0.52135	481.459	0.07
17	57.4635	1.11311	337.973	0.07
18	53.3785	5.90453	711.15	0.07
19	69.888	6.47599	732.044	0.07
20	32.076	6.29237	298.947	0.07
21	85.1094	0.30388	167.371	0.07
22	83.7128	8.49958	377.252	0.07
23	90.859	6.09754	353.315	0.07
24	60.1695	9.29915	95.8127	0.07
25	39.0758	8.10856	421.412	0.07
26	30.7074	5.13237	512.546	0.07
27	71.4696	7.47078	157.615	0.07
28	78.3673	5.28649	574.294	0.07
29	36.0555	4.27679	969.511	0.07
30	37.5359	0.72985	216.085	0.07
31	99.2156	3.7133	596.606	0.07
32	34.8473	8.70952	137.06	0.07
33	41.8959	3.07274	318.564	0.07
34	68.758	4.5203	39.3009	0.07
35	92.4145	8.90544	749.489	0.07
36	58.2816	9.6986	535.731	0.07
37	80.9365	8.28124	830.237	0.07
38	64.4876	2.86024	58.5293	0.07
39	75.5725	7.08613	633.311	0.07
40	**42.9633**	**9.14514**	**887.692**	**0.07**
41	54.3038	2.44738	117.113	0.07
42	88.0535	9.5292	276.435	0.07
43	47.2883	7.70246	237.959	0.07
44	86.6615	0.93096	952.216	0.07
45	40.2788	4.72951	768.567	0.07
46	72.7553	7.28652	497.588	0.07
47	50.4744	6.92554	911.761	0.07
48	56.3522	3.88108	810.75	0.07
49	97.9297	5.66506	250.829	0.07
50	**44.6047**	**0.1415**	**847.075**	**0.07**

ranging between 0 and 10 μs. These ranges were selected to be consistent with pressure values and rise times used in biomedical applications. Fig. 2 shows that the main difference between using (α_1, ω_1) and (α_2, ω_2) is the duration of the positive and negative pressure pulses, as well as the peak negative amplitude of both the first and the second pressure pulse. As shown in Fig. 3, changing p_2 in Eq. (3) modifies both the amplitude of the positive pressure peak and the amplitude of the negative pressure peak. This observation is relevant because in the literature, p is sometimes defined as the peak positive pressure amplitude (p^+), independent of the peak negative amplitude (p^-).

In this study, the delay was varied from 10 μs to a maximum value (Δt_{max}) that was adjusted for each p_s pulse. The minimum delay (10 μs) was chosen arbitrarily. Δt_{max} was defined as the time required for the bubble to collapse inertially for the first time, after being subjected to a single p_c pulse (Fig. 1). This maximum delay depends on α, ω and r_0. Running the simulation with $r_0 = 7\,\mu m$, its value was 267 and 969 μs for (α_1, ω_1) and (α_2, ω_2), respectively. With the large bubble ($r_0 = 70\,\mu m$), Δt_{max} was 286 and 1000 μs for α_1, ω_1 and α_2, ω_2, respectively.

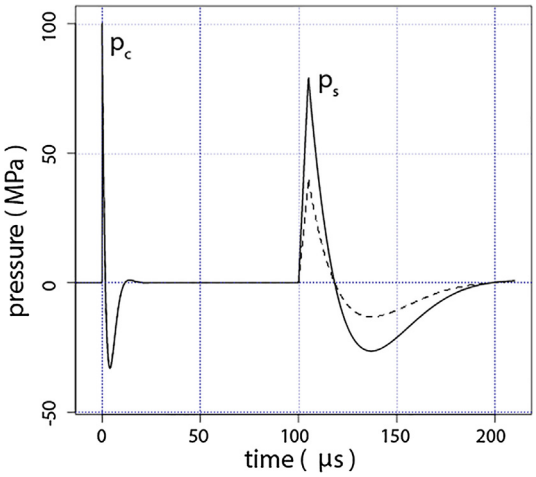

Fig. 3. Plots of two modified tandem shock waves, generated with Eqs. (2) and (3). In both cases, α_2 and ω_2 were used ($t_r = 5\,\mu s$). Two different values were selected for p_2: 80 MPa (continuous line) and 40 MPa (dashed line). For clarity, Δt was chosen to be 100 μs.

As in a previous publication [19], attention was focused on the minimum radius r_{min} achieved after the initial forced bubble collapse. In this research, the response variable $Y(\boldsymbol{x})$ to be modeled by Kriging was

$$Y(\boldsymbol{x}) = log_{10}[r_{min}(\boldsymbol{x})/r_0],$$

where $\boldsymbol{x} = (\Delta t, p_2, t_r)$. This variable was chosen because it was considered to be a measure of the capability of a pressure waveform to increase the collapse energy and, consequently, the microjet emission. Smaller $Y(\boldsymbol{x})$ values indicate that the pressure field produced a stronger bubble collapse. When using α_2 and ω_2, in most cases Y was evaluated at the third collapse, i.e., at the second inertial collapse. The flow diagram in Fig. 4 shows the step-by-step approach used in this study.

4. Results

4.1. Results obtained for an initial bubble radius of 7 μm

Sobol's indices of the response variable Y obtained for an initial bubble radius $r_0 = 7\,\mu m$ after the 50 runs are shown in Table 3. For both pairs of (α, ω) values, the results indicate that the most important factor (main effect) influencing bubble collapse is p_2. Only when using (α_2, ω_2), the sensitivity analysis reveals a significant interaction (0.2176) between p_2 and Δt. All other joint effects were not significant. Fig. 5 shows the prediction of 50 $\hat{Y}$-values obtained with the metamodel (fitted values) plotted against the exact values ("real" values Y) calculated using Eq. (1). Clearly, the estimated metamodel was better at predicting the results using (α_1, ω_1) than was using (α_2, ω_2), i.e., the values were closer to the 45° straight line. Furthermore, from Fig. 5(b), it is evident that for configurations number 5, 17, 41 and 46, the metamodel overestimated the response variable Y and that in configuration number 16 it underestimated Y.

The results achieved after running the metamodel 50,000 times are shown in Fig. 6(a) and (b). Each figure includes a global and a local color scale. Note that the color palette of both scales is the same. The global scale (right side) goes from the largest $\hat{Y}$ value (−1.8) to the smallest $\hat{Y}$ value (−2.6) obtained for all parameters considered in this article, that is, (α_1, ω_1), (α_2, ω_2), and the two initial bubble radii (7 and 70 μm). The local color scale only considers the maximum and minimum $\hat{Y}$ value obtained for the parameters corresponding to each specific case. There is no graph that includes all colors shown in the global scale. For instance, in Fig. 6(a), no red and blue tones appear because $\hat{Y}$ does not reach these values.

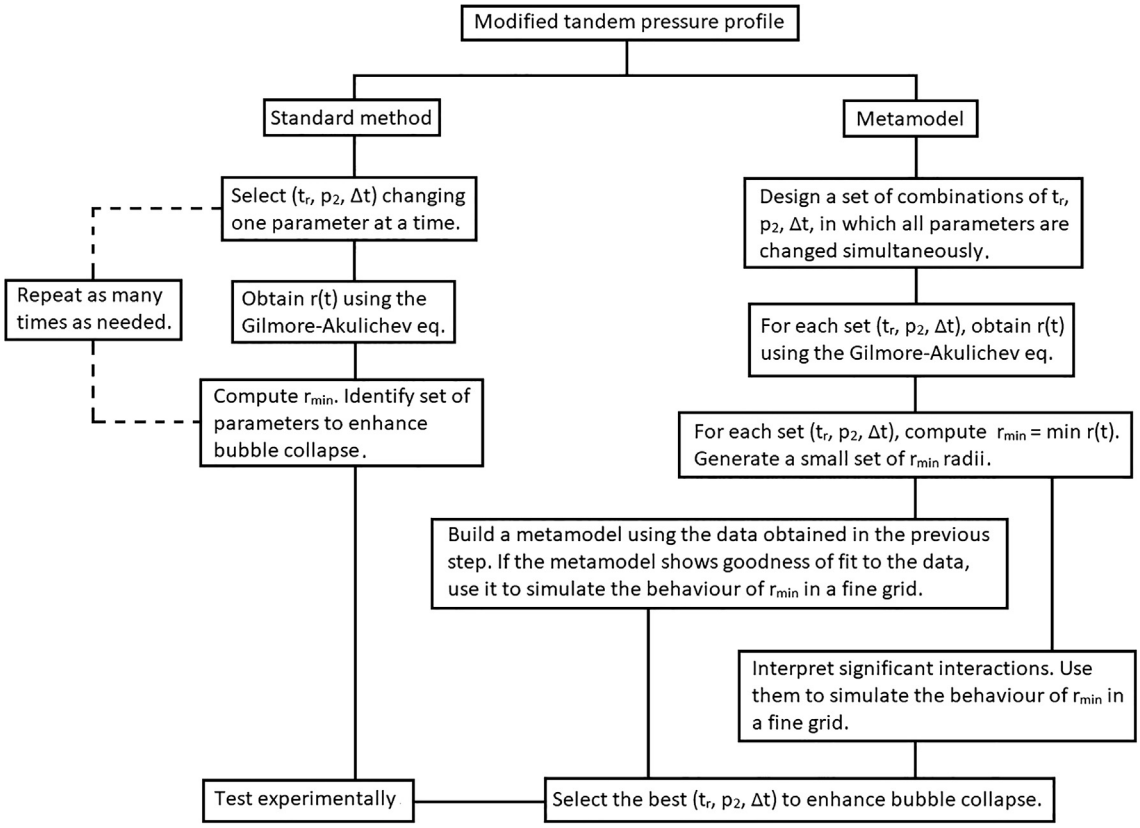

Fig. 4. Flow diagram showing the step-by-step approach used in this study (Kriging metamodel) compared to the standard method, where the differential equation is solved numerous times, changing one parameter at a time.

Table 3
Sobol's indices of the response variable $\hat{Y}$ obtained for an initial bubble radius $r_0 = 7$ μm after the 50 runs shown in Table 1.

α_1, ω_1	main effect	p_2 interaction	t_r interaction	Δt interaction
p_2	**0.8799**	–	0.0154	0.0148
t_r	0.0355	0.0154	–	0.0163
Δt	0.0148	0.0148	0.0163	–
α_2, ω_2	main effect	p_2 interaction	t_r interaction	Δt interaction
p_2	**0.4224**	–	0.0102	0.2176
t_r	0.0042	0.0102	–	0.0572
Δt	0.0264	**0.2176**	0.0572	–

Because the influence of the induction time was not significant, the response values estimated by the metamodel ($\hat{Y}$) were only plotted against p_2 and Δt. There is an obvious difference between using (α_1, ω_1) and (α_2, ω_2). In the case (α_1, ω_1), the estimated metamodel predicted that enhanced bubble collapse (low $\hat{Y}$ values) will be achieved using the highest possible p_2 at any desired delay between 10 and 267 μs. Surprisingly, when substituting the more realistic values (α_2, ω_2), the metamodel predicts improved results, i.e., smallest $\hat{Y}$ values (Fig. 6(b)), at high p_2 (more than approximately 80 MPa), and either short delays (between 10 and approximately 200 μs) or long delays (between approximately 800 and 970 μs).

4.2. Results obtained for an initial bubble radius of 70 μm

Estimating the metamodel using optimally selected $n = 50$ configurations for an initial bubble radius of 70 μm with the aforementioned p_2, t_r and Δt ranges (see Table 2) and both α and ω values, revealed that p_2 is the most important parameter affecting the response variable Y (see Table 4). As with the smaller bubble, there was a significant joint effect between p_2 and Δt when subjecting the bubble to the (α_2, ω_2)-pressure waveform. This interaction was stronger for the small bubble (0.2176 in Table 3) than that for the larger bubble (0.1543 in Table 4). All other joint effects were not significant. Fig. 7 reveals that, once again, the metamodel predicts bubble dynamics better for (α_1, ω_1) than that for (α_2, ω_2).

Fig. 8 shows the results obtained after running the metamodel 50,000 times by varying p_2, t_r and Δt in the aforementioned ranges. As in Fig. 6, a local and a global color scale were included in each figure. The influence of the induction time was not significant, and $\hat{Y}$ was only plotted against p_2 and Δt. Again, there was an evident difference between running the metamodel with (α_1, ω_1) and (α_2, ω_2). With the (α_1, ω_1)-waveform, the metamodel predicts that enhanced bubble collapse will be achieved using the highest possible p_2 at a relatively broad range of delays (10 to approximately 200 μs). As illustrated in Fig. 8(a), if the delay is increased, it becomes more important to also increase p_2. The best results are achieved at the shortest delay and highest p_2. When using α_2 and ω_2, the metamodel predicts that the best results can only be obtained at high p_2 (above approximately 90 MPa) and long delays (more than approximately 800 μs).

5. Discussion

The metamodel described in this article was useful for predicting ranges for the most convenient values of the input variables (Δt, p_2 and t_r) to enhance the collapse of a bubble subjected to a modified tandem shock wave. In other words, the metamodel predicted the parameters for which large negative $log_{10}\left(\frac{r_{min}}{r_0}\right)$ values can be expected. It was also helpful for determining the most important factor affecting bubble dynamics and for providing information on the joint effects between the input variables.

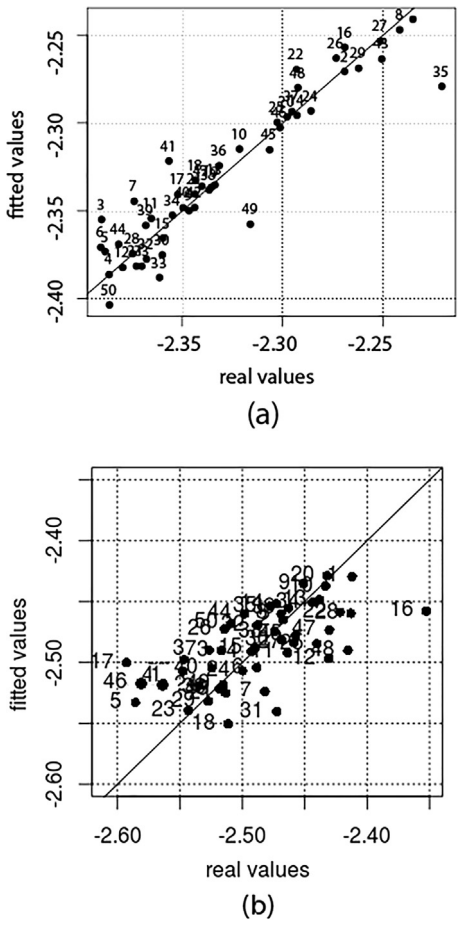

Fig. 5. Plot of 50 $\hat{Y}$ values obtained with the metamodel (fitted values) *vs* the exact values ("real" values) calculated using Eq. (1) for an initial bubble radius $r_0 = 7$ μm, using (a) α_1, ω_1, (b) α_2, ω_2.

The r_{min} radius was obtained by solving the differential equation that describes bubble dynamics. As the next step, r_{min} was modeled statistically. The quality of the statistical prediction depends on α and ω. Our results demonstrate that a simplified statistical model may adequately predict a phenomenon and be helpful for interpreting the significance of the parameters involved. In this case, only two parameters (Δt and p_2) were plotted because the model revealed that the induction time t_r does not have a significant influence on the response variable.

Even if a more realistic temporal pressure profile is obtained by using (α_2, ω_2), the old parameters (α_1, ω_1) were included in this study because many results and conclusions have been reported with this "classical" pressure pulse. Pressure waveforms modeled using α_1 and ω_1 fit pressure records obtained with needle polyvinylidene difluoride (PVDF) hydrophones very well [28]. Needle hydrophones were popular during the early days of clinical applications of shock waves and are still common in several research laboratories because they are relatively inexpensive, easy to use and provide reproducible results. A disadvantage of these pressure gauges is that the water–metal adhesion at the tip of the hydrophone does not withstand the tensile phase of a shock wave. Therefore, the amplitude and the duration of the negative pulse are underestimated. Fiber-optic hydrophones are well suited to registering underwater shock waves [29]; however, these systems are expensive and not as easy to use as PVDF gauges. Pressure waveforms obtained with fiber-optic hydrophones are modeled using α_2 and ω_2 in Eq. (2). The implications of using (α_1, ω_1) instead of (α_2, ω_2) should not be underestimated. Our results indicate that the use of (α_1, ω_1) may lead to incorrect conclusions. As shown in Figs. 6 and 8, as well as in Tables

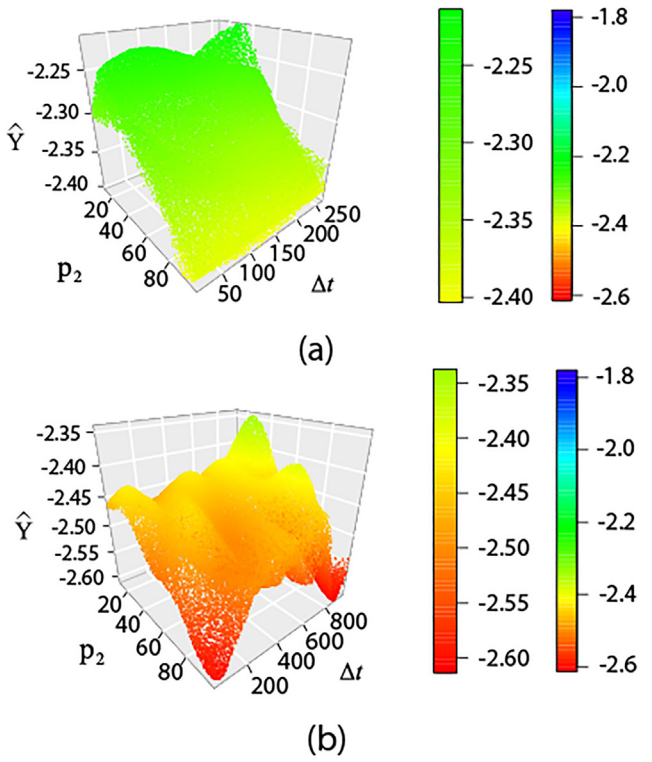

Fig. 6. Behavior of the response variable $\hat{Y}$ versus p_2 and the delay Δt, after running the metamodel 50,000 times, using an initial bubble radius r_0 of 7 μm, and (a) α_1, ω_1, (b) α_2, ω_2.

Table 4
Sobol's indices of the response variable $\hat{Y}$ obtained for an initial bubble radius $r_0 = 70$ μm after the 50 runs shown in Table 2.

α_1, ω_1	main effect	p_2 interaction	t_r interaction	Δt interaction
p_2	**0.8420**	–	0.0395	0.0042
t_r	0.0738	0.0395	–	0.0184
Δt	0.0132	0.0042	0.0184	–
α_2, ω_2	main effect	p_2 interaction	t_r interaction	Δt interaction
p_2	**0.5609**	–	0.0060	0.1543
t_r	0.0677	0.0060	–	0.0568
Δt	0.0903	**0.1543**	0.0568	–

3 and 4, a significant joint effect between p_2 and the delay was only observed with pressure waveforms modeled by substituting (α_2, ω_2) in Eqs. (2) and (3). These waveforms also produced much stronger bubble compressions than those obtained using (α_1, ω_1) (Figs. 6 and 8). A reason for this behavior is the much longer and "deeper" pressure trough that follows the positive phase of the p_s pressure pulse in Fig. 2(b) compared with that in Fig. 2(a). Using (α_2, ω_2), according to the metamodel high p_2 values and either short or long delays enhance the collapse of small bubbles (Fig. 6(b)); however, for a bubble with a radius that is ten times larger (Fig. 8(b)), only a long delay and high pressure will result in improved bubble collapse. Fig. 8(b) shows that this phenomenon does not influence the dynamics of the larger bubble.

Notably, it is impossible to anticipate the shape of the surfaces shown in Fig. 8(a) and (b) just by knowing the solutions of the differential equation. The statistical model and a large number of points (50,000) were required to construct both figures and show the details, including nonlinearities, of the surfaces along the whole three-dimensional space.

The results of numerical simulations could be a guide to adjusting

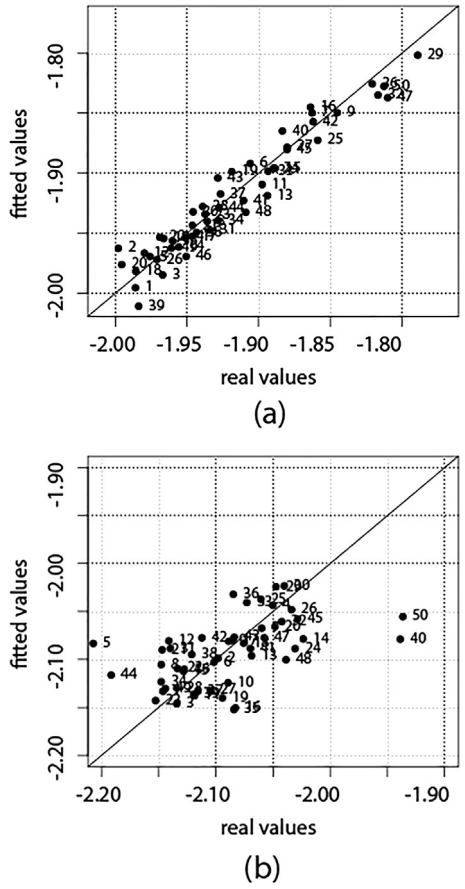

Fig. 7. Plot of 50 $\hat{Y}$ values obtained with the metamodel (fitted values) *vs* the exact values ("real" values) calculated using Eq. (1) for an initial bubble radius r_0 = 70 μm, using (a) α_1, ω_1, (b) α_2, ω_2.

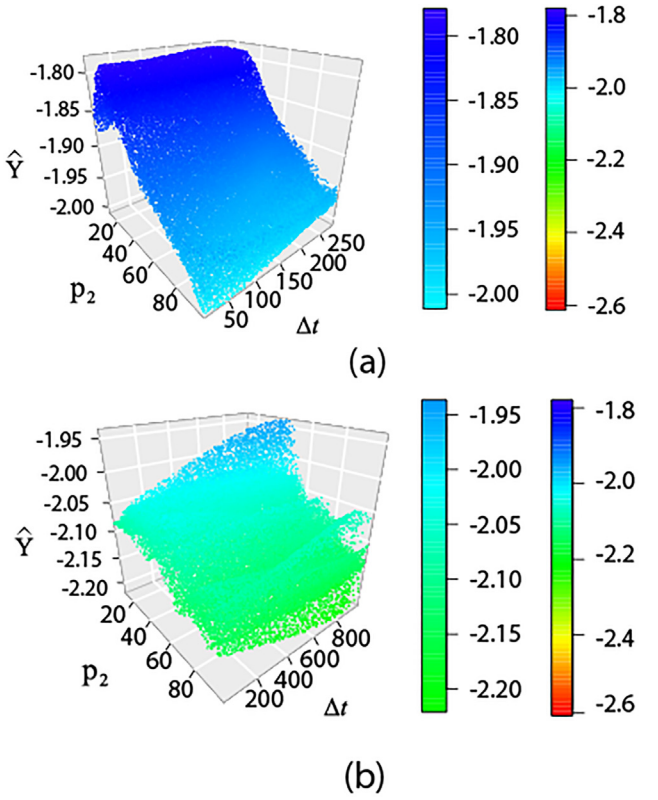

Fig. 8. Behavior of the response variable $\hat{Y}$ versus p_2 and the delay Δt, after running the metamodel 50,000 times, using an initial bubble radius r_0 of 70 μm, and (a) α_1, ω_1, (b) α_2, ω_2.

the parameters to improve the outcome of a physical experiment. Caution should be taken when interpreting p_2 as the peak positive pressure because, as previously mentioned, in our model, increasing p_2 increases not only the positive pressure pulse but also the absolute amplitude of the negative pulse (see Fig. 3). To a certain extent, increasing the voltage setting of a shock wave source produces shock waves with a larger amplitude of both the positive and the negative component.

Because the metamodel is an analytical expression, running it many times to predict the behavior of a response variable is easy. Running our surrogate model 50,000 times, to obtain images, such as those shown in Figs. 6 and 8, took fractions of a second on a conventional PC; however, solving Eq. (1) numerically several thousand times and changing the variables can be cumbersome. Moreover, the metamodel provides a panorama of bubble dynamics, analyzing several variables simultaneously. The results of the metamodel can be helpful for distinguishing significant joint effects. Specific numerical simulations to solve differential equations, such as Eq. (1), can be performed once these effects and the range of the variables of interest have been identified by the metamodel.

The surrogate model may also be used to predict the general behavior of a bubble subjected to single-pulse shock waves or to standard tandem shock waves. Furthermore, our methodology can be adapted to predict simulations based on equations different from the Gilmore-Akulichev formulation, such as the van der Waals equation. This simulation was not done because the main goal of this study was to evaluate if, in principle, a metamodel could be helpful for predicting the dynamics of a single air bubble subjected to shock waves. Future research could include more accurate and complicated expressions for predicting the bubble radius as a function of time.

The dynamics of a single spherical bubble immersed in water was chosen for simplicity. In a real scenario, bubbles tend to form clusters [6]. Nevertheless, the results obtained with single-bubble models may be useful for designing more efficient shock wave sources. The metamodel described here can simplify this task, providing information on how to optimize the efficiency of modified tandem shock waves. A metamodel could also be useful for predicting the behavior of multibubble fields, with associated nonspherical pulsations and coalescence, where changing several variables and solving the differential equations is much more challenging than that of the dynamics of a single spherical air bubble.

6. Conclusions

During the last two decades, the number of medical and biomedical applications of shock waves has been rapidly increasing. The most important phenomenon involved in desired and undesired effects of shock waves on cells and human tissue is acoustic cavitation, i.e., microbubble growth, collapse and high speed microjet emission. Shock wave-induced microjets significantly contribute to kidney stone pulverization during shock wave lithotripsy, produce transient pores in the membranes of human cells, bacteria and filamentous fungi, and convert biophysical stimuli into biochemical signals during extracorporeal shock wave therapy. Cavitation appears to stimulate the cells responsible for bone healing, as well as the cells in charge of the healing processes of connective tissues. Furthermore, microjets promote the resorption of calcium, thereby decreasing pain and improving function in patients suffering from tendon injuries. Studying the dynamics of microbubbles subjected to shock waves may help to design improved shock wave sources for specific clinical applications. Numerical simulations have been crucial to reducing experimentation time and costs;

however, the complexity of the phenomenon and the number of parameters and combinations involved result in long computation times. In this article, we demonstrate that using a well-known statistical model, such as Kriging, can be a helpful tool for studying the joint effect between the input variables, predicting the outcome, and significantly reducing the computation time. The metamodel can be used to study the influence of varying several input parameters of modified tandem shock waves on the collapse of a single air bubble immersed in water and to substitute time-consuming computer simulations based on the Gilmore-Akulichev equation with fast simulations created with the Kriging metamodel.

Acknowledgments

The authors extend special thanks to Francisco Fernández for useful discussion and careful revision of the manuscript. Guillermo Vázquez is acknowledged for technical assistance.

Funding

This research did not receive any specific grant from funding agencies in the public, commercial, or not-for-profit sectors.

Appendix A. Supplementary material

Supplementary data associated with this article can be found, in the online version, at https://doi.org/10.1016/j.ultras.2018.07.005.

References

[1] A.M. Loske, Medical and Biomedical Applications of Shock Waves, Springer Verlag, Cham, Switzerland, 2017 (Chap. 3, 4, 6, 7. ISBN 978-3-319-47568-4).
[2] R.O. Cleveland, J.A. McAteer, The physics of shock wave lithotripsy, in: A.D. Smith, G.H. Badlani, D.H. Bagley, R.V. Clayman, S.G. Docimo, G.H. Jordan, L.R. Kavoussi, B.R. Lee, J.E. Lingeman, G.M. Preminger, J.W. Segura (Eds.), Smith's Textbook on Endourology, BC Decker Inc, Hamilton, Ontario, Canada, 2007, pp. 317–332.
[3] P. Lukes, F. Fernández, J. Gutiérrez-Aceves, E. Fernández, U.M. Alvarez, P. Sunka, A.M. Loske, Tandem shock waves in medicine and biology: a review of potential applications and successes, Shock Waves 26 (2016) 1–23.
[4] L.A. Crum, Cavitation microjets as a contributory mechanism for renal calculi disintegration in ESWL, J. Urol. 140 (1988) 1587–1590.
[5] C.D. Ohl, R. Ikink, Shock-wave-induced jetting of micron-size bubble, Phys. Rev. Lett. 90 (2003) 214502-1–214502-4.
[6] M. Arora, L. Junge, C.D. Ohl, Cavitation cluster dynamics in shock-wave lithotripsy: part 1. Free field, Ultrasound Med. Biol. 31 (2005) 827–839.
[7] M.R. Bailey, Control of Acoustic Cavitation with Application to Lithotripsy, Applied Research Laboratories Report No: ARL-TR-97-1, The University of Texas at Austin, Austin, Texas and Defense Technical Information Center, 1997, p. 198.
[8] A.M. Loske, F.E. Prieto, J. Gutiérrez-Aceves, H. Zendejas, A. Saita, E. Velez, Evaluation of a bifocal reflector on a clinical lithotripter, J. Endourol. 18 (2004) 7–16.
[9] K.Z. Sheir, A.M. El-Sheikh, M.A. Ghoneim, Synchronous twin-pulse technique to improve efficacy of SWL: preliminary results of an experimental study, J. Endourol. 15 (2001) 965–974.
[10] D.L. Sokolov, M.R. Bailey, L.A. Crum, Use of a dual-pulse lithotripter to generate a localized and intensified cavitation field, J. Acoust. Soc. Am. 110 (2001) 1685–1695.
[11] P. Zhong, F.H. Cocks, I. Cioanta, G.M. Preminger, Controlled, forced collapse of cavitation bubbles for improved stone fragmentation during shock wave lithotripsy, J. Urol. 158 (1997) 2323–2328.
[12] Y. Zhou, F.H. Cocks, G.M. Preminger, P. Zhong, Innovations in shock wave lithotripsy technology: update in experimental studies, J. Urol. 172 (2004) 1892–1898.
[13] A.M. Loske, F.E. Prieto, F. Fernández, J. van Cauwelaert, Tandem shock wave cavitation enhancement for extracorporeal lithotripsy, Phys. Med. Biol. 47 (2002) 3945–3957.
[14] A.M. Loske, F. Fernández, H. Zendejas, M. Paredes, E. Castaño-Tostado, Dual pulse shock wave lithotripsy: in vitro and in vivo study, J. Urol. 174 (2005) 2388–2392.
[15] F. Fernández, G. Fernández, A.M. Loske, Treatment time reduction using tandem shock waves for lithotripsy: an in vivo study, J. Endourol. 23 (2009) 1247–1253.
[16] U.M. Álvarez, A. Ramírez, F. Fernández, A. Méndez, A.M. Loske, The influence of single-pulse and tandem shock waves on bacteria, Shock Waves 17 (2008) 441–447.
[17] A.M. Loske, J. Campos-Guillén, F. Fernández, E. Castaño-Tostado, Enhanced shock wave-assisted transformation of *Escherichia coli*, Ultrasound Med. Biol. 37 (2011) 501–510.
[18] A.M. Loske, F. Fernández, D. Magaña-Ortíz, N. Coconi-Linares, E. Ortíz-Vázquez, M.A. Gómez-Lim, Tandem shock waves to enhance genetic transformation of *Aspergillus niger*, Ultrasonics 54 (2014) 1656–1662.
[19] G. Canseco, M. de Icaza-Herrera, F. Fernández, A.M. Loske, Modified shock waves for extracorporeal shock wave lithotripsy: a simulation based on the Gilmore formulation, Ultrasonics 51 (2011) 803–810.
[20] R.O. Cleveland, O.A. Sapozhnikov, M.R. Bailey, L.A. Crum, A dual passive cavitation detector for localized detection of lithotripsy-induced cavitation in vitro, J. Acoust. Soc. Am. 107 (2000) 1745–1758.
[21] P.V. Chitnis, R.O. Cleveland, Quantitative measurements of acoustic emissions from cavitation at the surface of a stone in response to a lithotripter shock wave, J. Acoust. Soc. Am. 119 (2006) 1929–1932.
[22] M. de Icaza-Herrera, F. Fernández, A.M. Loske, Combined short and long-delay tandem shock waves to improve shock wave lithotripsy according to the Gilmore-Akulichev theory, Ultrasonics 58 (2015) 53–59.
[23] C.C. Church, A theoretical study of cavitation generated by an extracorporeal shock wave lithotripter, J. Acoust. Soc. Am. 86 (1989) 215–227.
[24] T.J. Matula, P.R. Hilmo, B.D. Storey, A.J. Szeri, Radial response of individual bubbles subjected to shock wave lithotripsy pulses in vitro, Phys. Fluids 14 (2002) 913–921.
[25] J.I. Iloreta, Y. Zhou, G.N. Sankin, P. Zhong, A.J. Szeri, Assessment of shock wave lithotripters via cavitation potential, Phys. Fluids 19 (2007) 086103-1–086103-16.
[26] K.T. Fang, R. Li, A. Sudjianto, Design and Modeling for Computer Experiments. Taylor & Francis Group, London, United Kingdom, 2006, pp. 78–90 (ISBN 978-1584885467).
[27] T. Hastie, R. Tibshirani, J. Friedman, The Elements of Statistical Learning: Data Mining, Inference and Prediction, Springer International Publishing AG, Cham, Switzerland, 2001, pp. 144–148 (ISBN 978-0-387-84857-0).
[28] M. Müller, M. Platte, Einsatz einer breitbandigen Drucksonde auf PVDF-Basis zur Untersuchung konvergierender Stosswellen in Wasser, Acustica 58 (1985) 215–222 (in German).
[29] J. Staudenraus, W. Eisenmenger, Fibre-optic hydrophone for ultrasonic and shock wave measurements in water, Ultrasonics 31 (1993) 267–273.